Materials and Design 189 (2020) 108526

Contents lists available at ScienceDirect

Materials and Design

journal homepage: www.elsevier.com/locate/matdes

The effect of grain size on the fatigue overload behaviour of nickel

Wen Zhang [a,*], Christopher A. Simpson [b], Pablo Lopez-Crespo [c], Mehdi Mokhtarishirazabad [b], Thomas Buslaps [d], Reinhard Pippan [e], Philip J. Withers [a,*]

[a] Henry Royce Institute, Department of Materials, The University of Manchester, Manchester M13 9PL, UK
[b] Department of Mechanical Engineering, University of Bristol, Queen's Building, University Walk, Bristol BS8 1TR, UK
[c] Department of Civil and Materials Engineering, University of Malaga, C/Dr Ortiz Ramos s/n, 29071 Malaga, Spain
[d] ESRF, 6 rue Jules Horowitz, Grenoble 38043, France
[e] Erich Schmid Institute of Materials Science, Austrian Academy of Sciences, Leoben, Austria

HIGHLIGHTS

- A setup for in-situ fatigue tests is established by applying synchrotron X-ray diffraction and digital image correlation.
- Grain size not only affects the baseline fatigue crack growth but also the fatigue overload behaviour of Ni.
- Various overload retardation mechanisms are investigated and explained.
- The *J*-integral and compliance methods for determining the crack driving force from the displacement field are developed.

GRAPHICAL ABSTRACT

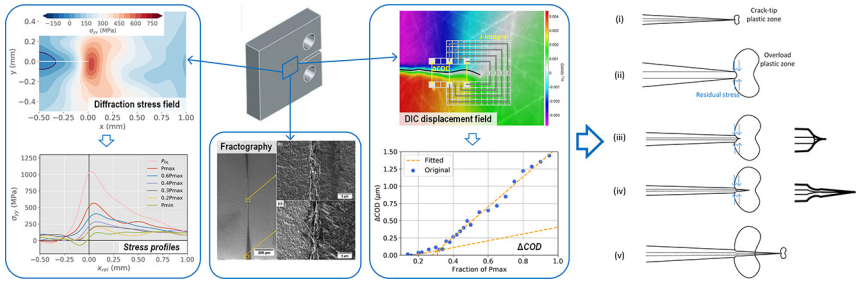

ARTICLE INFO

Article history:
Received 19 November 2019
Received in revised form 8 January 2020
Accepted 24 January 2020
Available online 25 January 2020

Keywords:
Nanocrystalline
Retardation mechanisms
Energy dispersive X-ray diffraction
Crack path
J-integral

ABSTRACT

The fatigue overload behaviours of coarse grain (~30 μm), ultrafine grain (360 nm) and nanocrystalline (~30 nm) Ni are compared under constant amplitude loading at $R = 0.1$ after a 100% overload. Synchrotron X-ray diffraction is applied to map the elastic crack-tip strain fields at the mid-thickness of a compact tension specimen of nanocrystalline Ni at various stages through the loading cycles, from which the variation in stress before, during and after overload is estimated. Digital image correlation is used to measure the crack length and the displacement fields at the specimen surfaces for both grain sizes, from which the fatigue crack growth (FCG) rate, crack opening displacement and stress intensity factor range are determined. The FCG for coarse grain Ni is most significantly retarded whereas the nanocrystalline Ni is least affected by the overload due to an increased yield stress and a more planar crack surface morphology. As a result, FCG retardation by plasticity, surface roughness and residual stress-induced crack closure are reduced.

1. Introduction

Fatigue performance is one of the most important properties for load bearing components and structures. It is well-known that fatigue crack growth (FCG) is dominated by the stress range and the mean stress [1–3]. In practice cracks generally experience variable amplitude fatigue cycling. Fatigue overloads can retard the FCG rate by reducing the

* Corresponding authors.
E-mail addresses: wen.zhang-10@postgrad.manchester.ac.uk (W. Zhang), p.j.withers@manchester.ac.uk (P.J. Withers).

https://doi.org/10.1016/j.matdes.2020.108526

effective stress intensity factor (SIF) range as well as the mean stress intensity due to the combined effect of various retardation mechanisms. These include plasticity-induced crack closure, residual stress, crack deflection and surface roughness.

Plasticity-induced closure [4–10] and residual stress [11–13] are believed to be the primary causes for the fatigue overload retardation phenomenon. The application of an overload introduces a significant shape misfit between the plastically stretched material around the crack tip and the rest of the material in the elastic regime. As a consequence, a compressive zone is generated during unloading. This compressive residual stress lowers the stress acting on the crack and hence the local mean stress. Immediately after overload the plastic stretch means that the crack flanks are too far apart to come into contact during unloading. However, as the crack grows past the overload the opposing 'humps' on the crack faces caused by the plastic stretch can cause the crack faces to touch before reaching the minimum load. This reduces the effective stress range and therefore slows crack propagation. Under certain circumstances when the R ratio is low, if the residual compressive stress is large enough, it can compress the crack faces into contact [14], which gives rise to residual stress induced crack closure. In this case, residual stress can reduce not only the mean stress, but also the stress range.

Crack deflection [15,16] can play an important role especially when the crack does not grow straightly or perpendicular to the loading direction as observed in ultra-fine grained Ni produced by severe plastic deformation [17–19]. The deflected crack reduces the effective SIF range and enhances the local Mode II component. This leads to the relative lateral movement of the crack surfaces along the crack growth direction and thus facilitates roughness-induced crack closure at low stress levels [20–23]. Roughness-induced crack closure as a secondary effect can be reinforced by plasticity-induced closure, residual stress and crack deflection, which makes it an important influence factor for crack growth retardation when different degrees of crack tortuosity for materials of various grain sizes are taken into account.

A long-term endeavour for materials science is to seek approaches to strengthen materials without significantly reducing their ductility and toughness, but these design aspirations are normally at odds with one another. Nanocrystalline (NC) materials have attracted attention due to the very high strength, strength-to-weight ratio, fatigue life and wear resistance [17]. These superior properties generate great interest in a variety of structural and functional applications (such as in aerospace, transportation, medical devices and sports product) [24]. However, grain refinement that generally increases the strength whereas reduces the toughness of the material [25] can diminish the plasticity that could be introduced into the crack-tip region. Thus the effects of overload-induced crack closure and residual stress are correspondingly decreased. Besides, a smaller grain size can lead to a straighter crack with lower surface roughness [14,16], which reduces the effects of crack tortuosity and roughness-induced crack closure and hence lessens the fatigue overload retardation effects. All these effects arising from grain refinement put it under doubt that whether fatigue overload can retard the FCG for NC material and what the corresponding retardation mechanisms are.

A number of studies have started to look at the fatigue crack growth of nanocrystalline materials [26–28]. In particular, Steuwer et al. [12] studied a fatigue overload experiment on an ultra-fine grained (UFG) aluminum alloy at low stress ratio ($R = 0.1$) under plane strain conditions with synchrotron X-ray diffraction. They observed significant compressive residual stress immediately following the overload event while crack closure was not evident. They attributed the absence of crack closure to the plane strain conditions and the very small overload-induced plastic zone. Crack closure is believed to be promoted by plane stress over plane strain [29]. Unfortunately crack growth rates were not recorded in their study and so it is unclear what effect this residual stress had on the crack growth. Our previous fatigue overload study [14] on ultrafine grained (UFG) Ni (grain size ~360 nm) at $R = 0.1$ under plane strain with synchrotron X-ray diffraction (SXRD) and digital image correlation (DIC) showed retardation due to the combined effects of crack closure and residual stress. However, little has been reported in literature on the fatigue overload behavior of NC material, possibly due to the difficulty in producing NC material large enough for mechanical testing. Thus, it is pertinent to ask whether such overload retardation effects are evident for NC nickel (grain size ~30 nm).

In this study, a fatigue overload experiment was conducted on the NC Ni produced by pulsed electrodeposition with the same sample geometry and loading conditions as used in our previous study on UFG Ni [14]. Energy dispersive synchrotron X-ray diffraction (EDXRD) and DIC were applied to measure the fatigue behaviours in the bulk (plane strain) and at the surface (plane stress) respectively. The evolution of stresses around the crack tip prior to, during and after overload was estimated by EDXRD and the crack opening displacement (ΔCOD) and stress intensity factor range (ΔK) were determined through the DIC displacement field. As a systematic comparison covering the whole range of the grain sizes, a lab fatigue overload experiment with DIC was also conducted on coarse grained (CG) nickel (grain size ~30 μm) under the same loading conditions as the NC and UFG samples. All the samples were fractured after the fatigue tests for surface roughness measurements and fractography analysis.

2. Experimental methods

2.1. Material and experimental procedure

A compact tension (CT) sample geometry was applied for both NC and CG Ni. The NC samples were machined from plates produced by pulsed electrodeposition. The CG samples were taken from the as-received 99.99% purity Ni from Goodfellow™. Some of the key properties and loading conditions are listed in Table 1. The sample geometry

Table 1
Material properties, specimen dimensions, cyclic loading and estimated plastic zone sizes for the Ni specimens of various grain sizes.

	NC Ni	CG Ni	UFG Ni low k_{II}	UFG Ni high k_{II}
Production route	Pulsed electrodeposition	As received	High pressure torsion	
Grain size	30 nm	30 μm	280 × 550 nm^2	
Yield strength (MPa)	1200	385	800	
Width, W (mm)	5.18	16	5.22	5.30
Thickness, B (mm)	1.34	1.92	1.48	1.20
Load, P (N)	16–160	50–500	20–200	16.6–165.6
Overload, P_{OL} (N)	320	1000	400	331.2
ΔK at OL-1 (MPam$^{0.5}$)	10.6	11.6	11.7	10.3
ΔK at OL (MPam$^{0.5}$)	23.4	25.9	24.6	21.6
Overload forward plastic zone, r_p^{OL} (μm)	120	1440	341.8	331.2
Overload cyclic plastic zone, r_c (μm)	27.4	325.2	77.1	74.7

Note: The data for the UFG specimens is taken from [14]. The plastic zone sizes are estimated by Irwin's model [30].

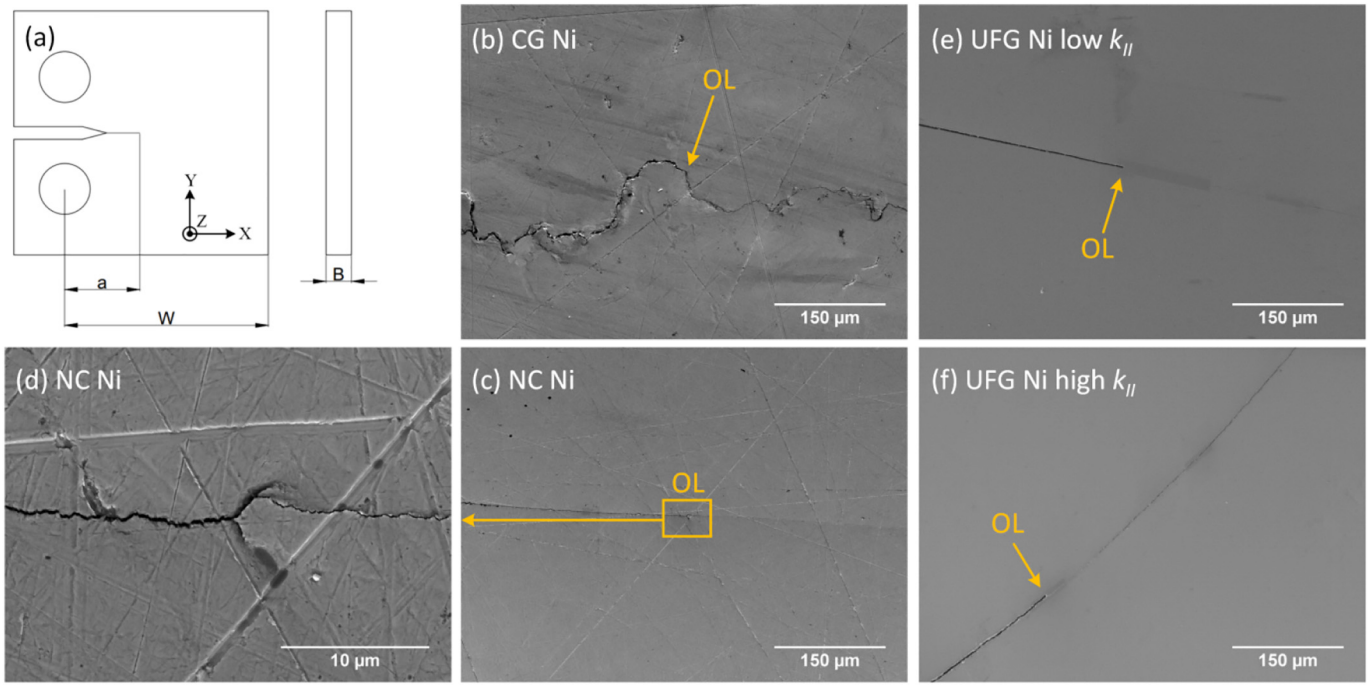

Fig. 1. (a) Geometry for compact tension samples (see Table 1). SEM images of the cracks for (b) CG Ni and (c) NC Ni. (d) High magnification showing the overload position in (c). (e) Low k_{II} and (f) high k_{II} cases of UFG Ni, which are taken from [14]. The crack propagation direction is from left to right.

and the morphology of the cracks are shown in Fig. 1. For CG and NC Ni samples, the crack growth followed the symmetry plane of the test-pieces. However, the crack propagation direction for both UFG specimens, cut in different orientations from a high pressure torsion disc, deflected slightly (Fig. 1e) and significantly (Fig. 1f) to the specimen symmetry plane, which are therefore referred to as low k_{II} and high k_{II} specimens respectively [14]. The dimension for the NC sample is similar to that for the UFG samples in our previous study [14] while the CG sample is much larger. This is to ensure the sample is significantly larger than the grain size such that the overall FCG rate is macroscopically representative.

Constant loading amplitude at a frequency of 40 Hz at $R = 0.1$ ($P_{min}/P_{max} = 0.1$) was applied on the samples during baseline fatigue cycling. A 100% overload ($P_{OL} = 2P_{max}$) was applied at a crack length such that a similar overload SIF range was experienced by all the samples of various grain sizes as shown in Table 1.

EDXRD and DIC measurements were made at fatigue stages prior to, during and after overload in order to capture the change and evolution in the fatigue behaviour caused by the overload event. The images taken by the DIC camera were also used to determine the crack lengths.

The in-situ overload fatigue experiment on NC Ni was conducted on beamline ID15A at the European Synchrotron Radiation Facility (ESRF, Grenoble, France) with EDXRD and DIC. The schematic of the setup is shown in Fig. 2. A 3 kN BOSE fatigue rig was mounted on the beamline sample table. A DIC camera with two ×2 teleconverters was fixed to a stepper motor such that it could be moved into the line of beam (with

Fig. 2. Setup for the in-situ fatigue overload experiment with energy dispersive X-ray diffraction and digital image correlation on beamline ID 15A at the ESRF. The coordinate system for the lab frame (X, Y, Z) is shown in the figure.

the beam off) to image the specimen surface. Two X-ray detectors were mounted on the other side of the specimen to collect diffraction signals at $2\theta = 5°$, one horizontally and one vertically off-set. This setup enables X-ray and DIC measurements at the same loading levels of each fatigue stage of interest. X-ray diffraction was applied to investigate five fatigue stages, namely OL-1, OL, OL+1, OL+1100 and OL+3100. In this notation OL represents the cycle count at which the overload event occurred, while the number of cycles, X, before or after the overload is described as OL-X or OL+X respectively. Within each stage, 2D strain/stress maps were acquired at P_{max} and P_{min} while line profiles were obtained at the intermediate loading levels so as to collect data in a time efficient manner. The details for the map and line scans are summarised in the following section.

Due to the large grain size of CG Ni, and hence bad grain sampling statistics within the small gauge volume, synchrotron X-ray diffraction measurement could not be performed on the CG sample. Nevertheless the lab. fatigue experiment monitored by DIC combined with post-mortem fractography and roughness analysis was able to give good insight into the overload effect on CG Ni. Due to the limited beamtime and the challenge to characterize the very small plastic zone for the NC sample, the ESRF experiment was repeated in the lab. with more time-consuming and more detailed DIC measurements. To be specific, additional fatigue stages were investigated by DIC than X-ray diffraction to better define the evolution of the overload behaviour. Within each stage of fatigue cycling, 25 and 31 load levels from P_{max} to P_{min} were monitored by DIC for NC and CG Ni respectively, from which ΔCOD and ΔK were estimated.

2.2. Energy dispersive X-ray diffraction

A polychromatic beam (collimated to $25 \times 25\ \mu m^2$) was used to map the crack-tip strain fields at various fatigue stages prior to, during and after overload. The diffracted beam was captured by two detectors at a scattering take-off angle, $2\theta = 5°$. The horizontally off-set detector (with the horizontal opening of the detector collimator slits being 50 μm) measured the strains in the crack opening direction (ε_{yy}) while the vertically off-set detector (with the vertical opening of the detector collimator slits being 50 μm) measured the strains along the crack propagation direction (ε_{xx}). To ensure the gauge volume was positioned at the mid-thickness, the sample was first translated along the beam direction (Z direction in Fig. 2) to determine the Z-coordinate for which the gauge entered and exited the sample. This line scanning method was also used to accurately determine the position of notch-tip. The current crack-tip position and hence the relative distance between it and the notch tip were determined from the DIC analysis.

At each fatigue cycle of interest, a 2D map consisting of a fine map (25 μm spaced) just around the crack tip and a coarse map (spaced by 160 μm) further away from the crack tip was acquired at P_{max} and P_{min}. Line profiles composed of a band of fine and coarse lines similar to the maps were acquired at intermediate levels ($0.6P_{max}$, $0.4P_{max}$, $0.3P_{max}$ and $0.2P_{max}$) during unloading.

The elastic strain can be determined by

$$\varepsilon^{hkl} = \frac{d^{hkl} - d_0^{hkl}}{d_0^{hkl}} \tag{1}$$

where d_0^{hkl} is the stress-free lattice spacing of the (hkl) plane and d_{hkl} is the measured spacing. There exist many methods to determine the stress-free d_0 value [31]. In this study, d_0 is determined at a location that is far away from the crack (close to the corner on the tested samples) with no externally applied load. For FCC structured Ni, (311) is one of the lattice planes that are least affected by the intergranular stresses [32] and was therefore chosen to calculate the strain [33]. The strain estimation and the merging of the fine and coarse maps were then performed using the pyXe strain analysis package [34].

The stress distribution around the crack tip in the mid-thickness of the sample under plane strain conditions can then be evaluated by

$$\sigma_{yy} = \frac{E^{hkl}}{(1+\nu^{hkl})(1-2\nu^{hkl})}\left(\nu^{hkl}\varepsilon_{xx}^{hkl} + \left(1-\nu^{hkl}\right)\varepsilon_{yy}^{hkl}\right) \tag{2}$$

where the elastic modulus $E^{311} = 185$ GPa and the Poisson's ratio $\nu^{311} = 0.33$ following the Kroner polycrystal modelling scheme [32].

2.3. Digital image correlation

Random and fine scratch patterns were generated on the sample surfaces with grinding paper from 600 up to 2000. For the DIC measurements on the CG sample, one teleconverter was used giving a field of view of $6.61 \times 6.61\ mm^2$ and a pixel size of 3 μm. For the NC sample, two teleconverters were used to give a field of view of $3.28 \times 3.28\ mm^2$ and a pixel size of 1.6 μm. The commercial software LaVision DaVis was used to process the images. For each fatigue stage, all the images were correlated to the one at P_{min}. An interrogation window of 32 × 32 pixels with 75% overlap (8 pixels spacing between neighbouring windows) was used to obtain the displacement fields for both samples. The ΔCOD at various distances from the crack tip was calculated by the subtracting the displacements (in the crack opening direction) of the upper and lower crack flanks (as shown in Fig. 3).

Another important fracture mechanics parameter, the J-integral [35], can also be extracted from the elastic region of the displacement field (as shown in Fig. 3):

$$J = \int_{\Gamma}\left(wdy - \vec{T}_i\frac{\partial \vec{u}_i}{\partial x}ds\right) \tag{3}$$

where

Γ: represents a counter-clockwise path
w: strain energy density. $w = \int_0^{\varepsilon_{ij}}\sigma_{ij}d\varepsilon_{ij}$
$\vec{T}_i$: traction vector. $\vec{T}_i = \sigma_{ij}n_j$
$\vec{u}_i$: displacement vector
d_s: length increment along the contour

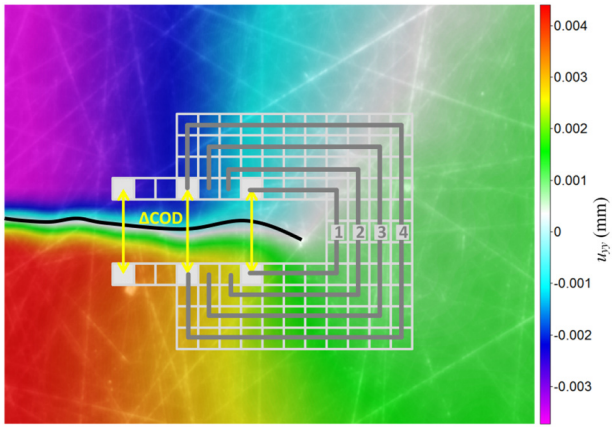

Fig. 3. Displacement field (color map) on top of the scratched sample surface. The crack is denoted by the black curve. The crack opening displacement at various locations behind the crack tip can be estimated by subtracting the vertical displacements of the upper and lower flanks of the crack as indicated by the yellow arrows. The gray paths describe the contours for determining the J-integral. The interrogation windows are shown by the white grids.

The J-integral is path independent and can be related to the SIF in an elastic field (linear elastic fracture mechanics conditions) [30]:

$$K_I = \sqrt{JE'} \tag{4}$$

where $E' = E$ for plane stress and $E' = E/(1\text{-}\nu^2)$ for plane strain.

A routine for calculating the J-integral from the displacement field was implemented using Python code. The procedure and verification of this routine can be found in Appendix A.

3. Results

3.1. Fatigue crack growth results

For a CT specimen, the nominal mode I SIF can be estimated as follows [36]:

$$\Delta K = \frac{\Delta P}{B\sqrt{W}} \frac{(2+\alpha)}{(1-\alpha)^{1.5}} (0.886 + 4.64\alpha - 13.32\alpha^2 + 14.72\alpha^3 - 5.6\alpha^4) \tag{5}$$

where $\alpha = a/W$. All the geometrical parameters are indicated in Fig. 1a.

The same loading conditions were applied to all the Ni specimens. For all the FCG data, the remaining ligament (W-a) is larger than $(4/\pi)(K_{max}/\sigma_y)^2$ such that linear elastic fracture mechanics (LEFM) is applicable. To eliminate short crack effects, the crack length a is $>2.5(K_{max}/\sigma_y)^2$. The thickness for the NC and UFG Ni specimens complies with the condition $B > 2.5(K_{max}/\sigma_y)^2$ [37] such that plane strain prevails. For CG Ni, the specimen thickness is slightly smaller than $2.5(K_{max}/\sigma_y)^2$, which may lead to a stress state residing between plane strain and plane stress.

Overall the crack paths for the NC and CG specimens are perpendicular to the loading direction. However, it is evident from Fig. 1 that the crack for NC Ni is very straight while that for CG Ni is very tortuous.

Fig. 4 delineates the FCG results for the NC and CG specimens alongside the UFG results (taken from [14]) for comparison purposes. The baseline (before overload and well after overload) FCG rate for the low k_{II} case of UFG Ni is the largest among the four while for CG and the high k_{II} case of UFG specimens the FCG rates are comparatively small. The straight crack path and elongated microstructure (with the elongation orientation approximately perpendicular to the loading direction) contributes to the fast crack propagation for the low k_{II} case of UFG Ni, while the significantly deflected crack for the high k_{II} case of UFG Ni and crack tortuosity for CG Ni provide resistance to the FCG. When the overload was applied, the most significant retardation in FCG is observed in the CG specimen in terms of the decrease in FCG rate and the retardation distance, while only a transient drop in FCG rate is observed for the NC specimen. This is because the plastic zone (listed in Table 1) is significantly larger for the CG specimen than for the NC specimen. A very small plastic zone can only generate a very limited level of crack closure and compressive residual stress, which does not significantly retard the FCG.

3.2. Energy dispersive X-ray diffraction results

The plane strain stress maps for the crack opening direction for the NC specimen prior to, during and after overload are shown in Fig. 5. The line profiles extracted from the stress maps and line scans along the crack plane are shown in Fig. 6, which makes it easier for quantitative analysis and comparison. The stress profiles for the high k_{II} case of UFG Ni [14,38] are also included in Fig. 6 for ease of comparison.

As shown in Figs. 5 and 6, the peak crack-tip stresses in the crack opening direction reached at P_{max} are slightly reduced after the application of the overload. This reduction is observed to occur until stage OL +1100, with stresses having recovered by stage OL+3100. This is due to the effect of residual stress and is also reflected in Fig. 4 with the FCG rate for the NC specimen being transiently and slightly retarded. However, the decrease in the stresses at P_{min} after overload is not evident since the overload cyclic plastic zone is small at just 27.4 μm (as detailed in Table 1). For the high k_{II} case of UFG Ni, a marked decrease in the stresses at both P_{max} and P_{min} occurs after overload (see Fig. 6(g and h)), with significant compressive stress observed ahead of the crack tip at P_{min} of the overload cycle (Fig. 6g). This indicates a more prominent residual stress effect for the UFG specimen than for the NC one.

Moreover, for the high k_{II} case of UFG Ni, the stress in the wake of the crack tip at P_{min} is still very compressive 19,000 cycles after overload (Fig. 6h) compared with OL-1 (Fig. 6f), especially at the overload location. This indicates crack face contact at the overload location when the crack has propagated around 200 μm past overload. However, no evident change in the stresses at P_{min} is observed for the NC specimen before and after overload, which means that crack closure is not measured by X-ray diffraction. The very high strength of the NC specimen restricts crack-tip plastic deformation and stretching by the overload such that premature crack face contact was not observed during unloading. This is in spite of the utilisation of a very small beam size (25×25 μm^2) in the region around the crack tip and due to the fact that the cyclic plastic zone is similar in size to the gauge volume.

3.3. Digital image correlation results

As discussed in Section 3.2, the stress fields measured by synchrotron X-ray diffraction in the bulk of the NC specimen under plane strain

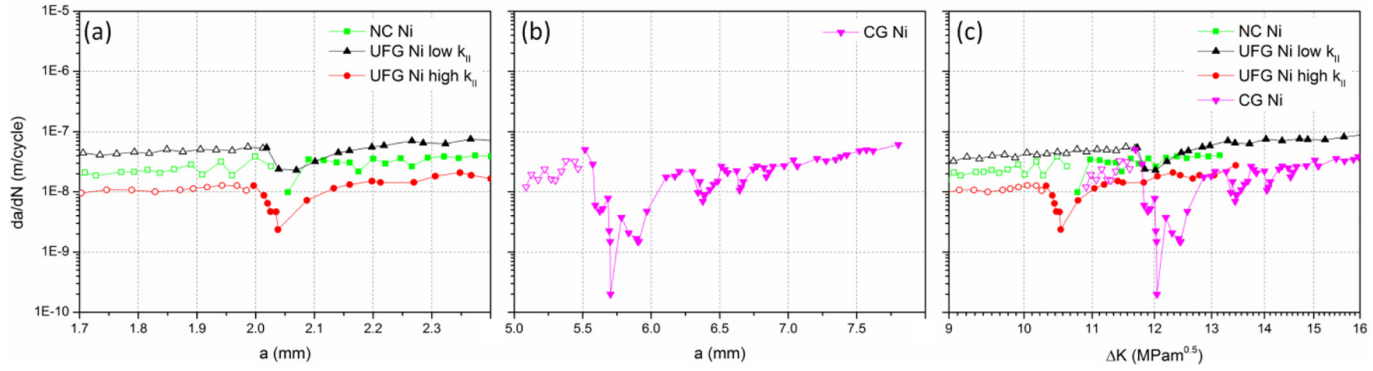

Fig. 4. Fatigue crack growth curves. Variation in fatigue crack growth rate, da/dN, with respect to crack length, a, for (a) NC, the high and low k_{II} cases of UFG Ni and (b) CG Ni. (c) Variation in da/dN with respect to the stress intensity factor range for all the nickel specimens. The FCG results for the UFG specimens are taken from [14]. Hollow markers highlight FCG rates prior to overload.

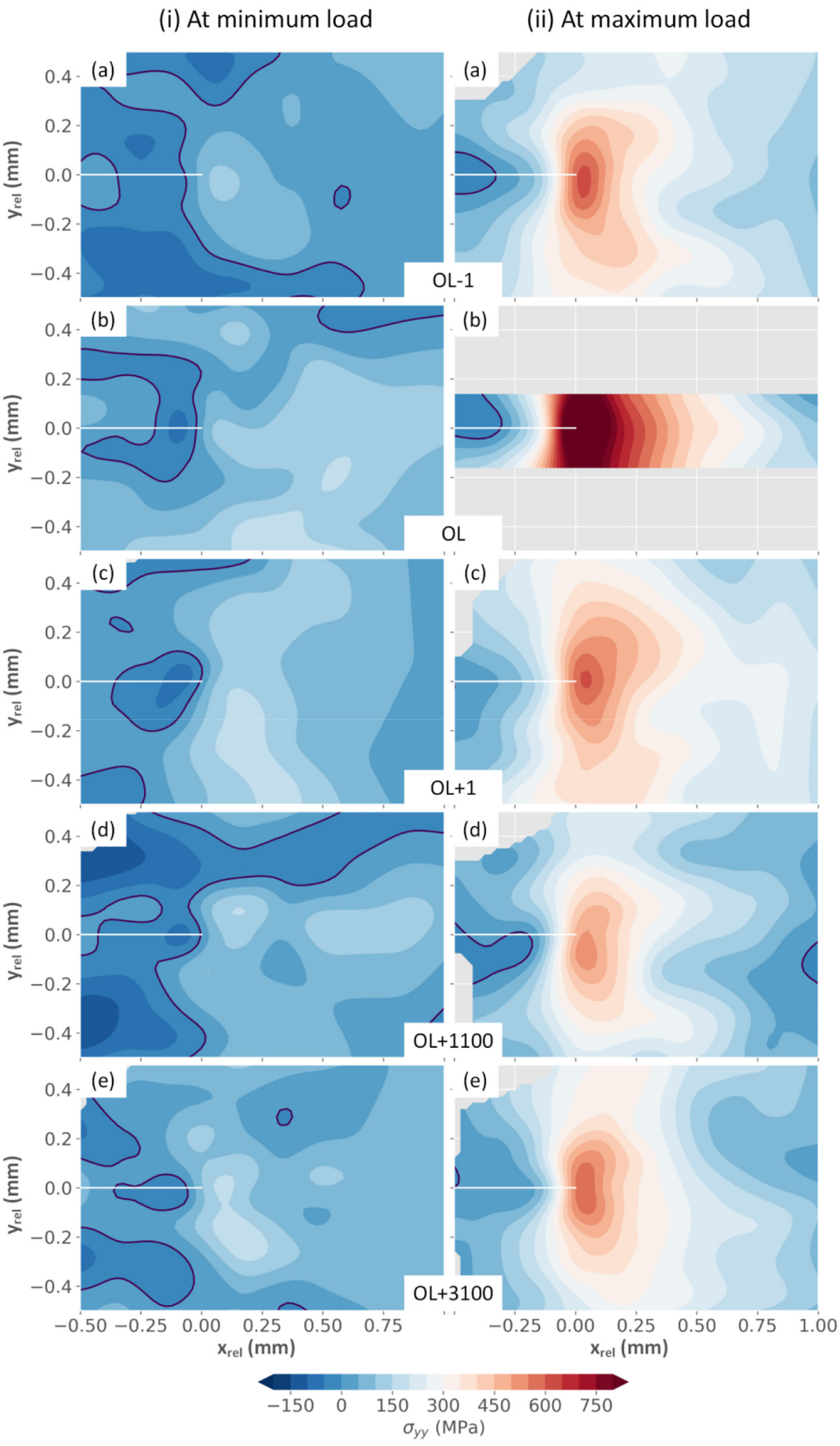
(i) At minimum load
(ii) At maximum load
(a)
(b)
(c)
(d)
(e)
OL-1
OL
OL+1
OL+1100
OL+3100
y_{rel} (mm)
x_{rel} (mm)
0.4
0.2
0.0
−0.2
−0.4
−0.50 −0.25 0.00 0.25 0.50 0.75
−0.25 0.00 0.25 0.50 0.75 1.00
−150 0 150 300 450 600 750
σ_{yy} (MPa)

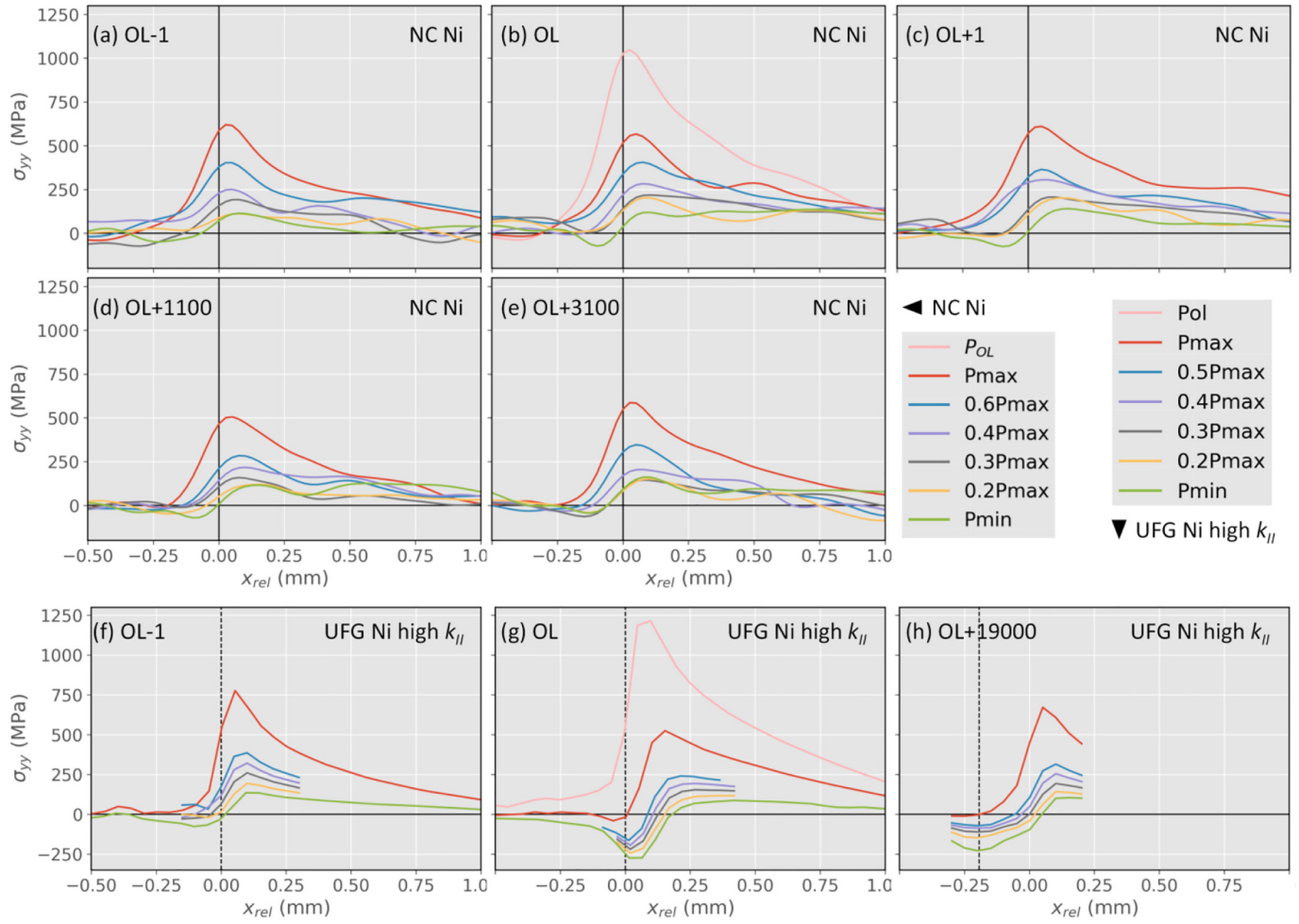

Fig. 6. Line profiles of the stresses in the crack opening direction along the crack faces for the NC specimen and the high k_{II} case of UFG Ni before, during and after overload. The horizontal coordinate (x_{rel}) denotes the relative distance to the current crack-tip position. The results for the UFG specimen are taken from [14,38]. The vertical dashed lines in (f, g and h) denote the overload location.

conditions show only a slight residual stress effect induced by the overload. Digital image correlation was used to study the surface behaviour of the NC as well as the CG specimens under plane stress by estimating the crack opening displacement and stress intensity factor range from the displacement fields. Additional fatigue stages were also investigated to give a detailed picture of the evolution of the overload effect.

3.3.1. Crack opening displacement

The variation in crack opening displacement (ΔCOD) extracted from the displacement fields (illustrated in Fig. 3) with respect to the fraction of the maximum load at fatigue stages before, during and after overload at increasing distances behind the crack tip for the CG and NC specimens are shown in Figs. 7 and 8, respectively. The change in ΔCOD should be proportional to the external load if crack closure is absent. Traditionally crack face contact can be identified by a distinct change in slope (sometimes called the 'closure knee') in the compliance curve by using a back-face strain gauge [36,39]. Here DIC is applied using the same principle to determine the existence of crack closure.

For the CG specimen (Fig. 7), a dramatic change in the slope is not observed immediately after overload but rather only after the crack has propagated ~140 μm beyond the overload position. This is because the plastic stretch induced by the overload is so significant that the retardation effects such as plasticity-induced crack closure and residual stress are suppressed. This is called 'delayed retardation' by some researchers [40–42] and is evidenced in Fig. 4 for CG Ni. As the crack propagates further into the overload plastic zone, the closure knee starts to develop at higher load. The crack closure effect is most pronounced after ~132,000 cycles beyond overload when the crack has grown ~420 μm from the overload position where the change in slope occurs at the highest fraction of the load, where $P = 0.6P_{max}$. After this the crack face contact gradually reduces towards that corresponding to the baseline state. The evolution of the overload effect for the CG specimen is in common with that for the UFG specimens [14], which points to the combined effect of plasticity-induced crack closure and residual stress (discussed in detail in Section 4.1).

By contrast, for the NC specimen in Fig. 8, a 'closure knee' is not observed. As is described in Section 2.3, 8 pixels spacing between correlation windows with a pixel size of 1.6 μm for NC Ni gives a spacing of 13 μm for the displacement matrices. It has also been observed in Fig. 7 that the closer the ΔCOD is extracted from the crack tip the more evident is the 'closure knee'. The 13 μm spacing however does not allow the ΔCOD to be accurately extracted from the displacement field within microns from the crack tip where slight crack face contact might occur.

Fig. 5. Crack-tip stress fields for the crack opening direction σ_{yy} after various numbers of fatigue cycles relative to the overload cycle for NC Ni at (i) minimum load and (ii) maximum load. The coordinates (x_{rel} and y_{rel}) describe the relative distance to the current crack-tip position. The white lines denote the current crack positions.

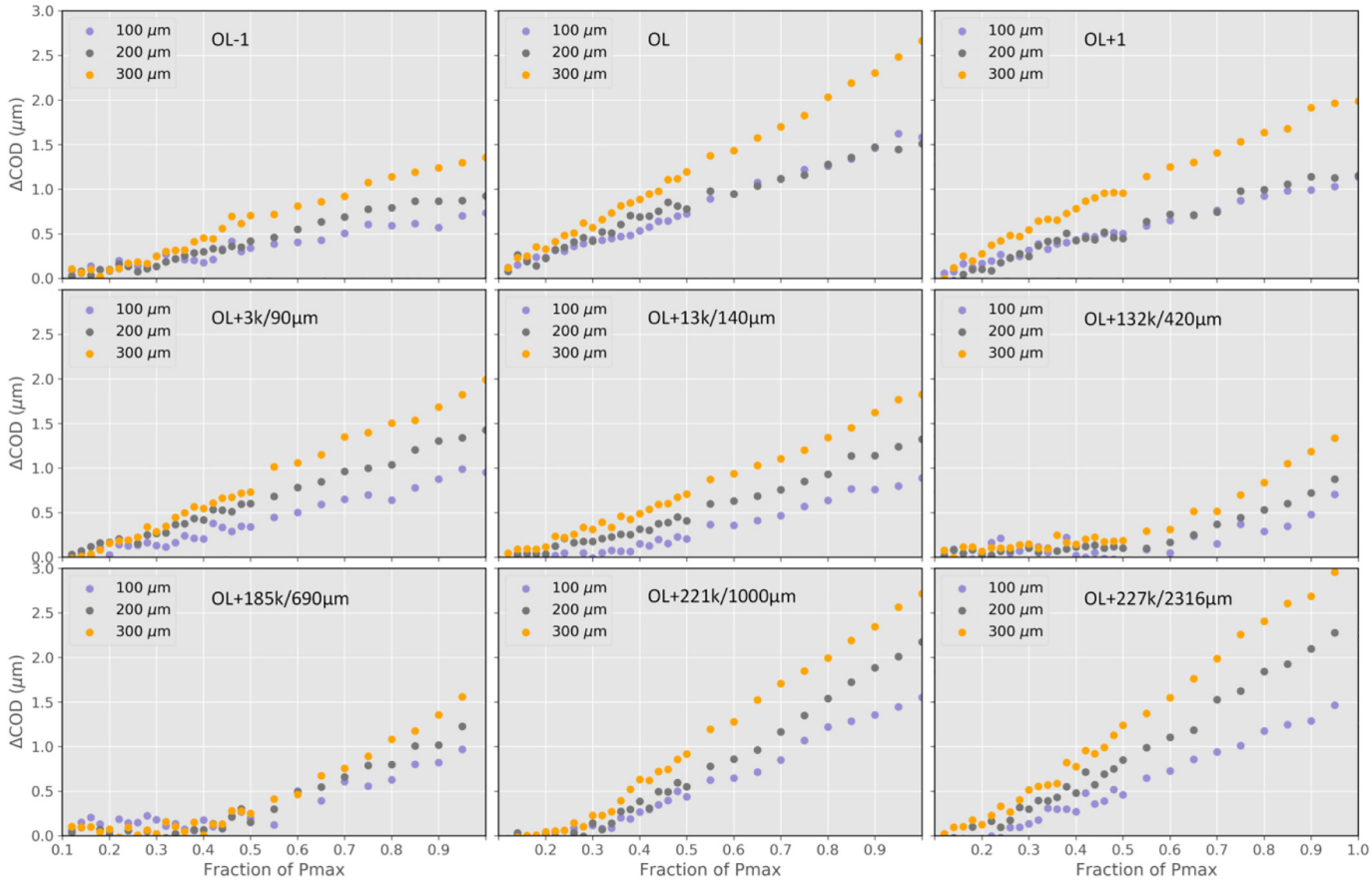

Fig. 7. Crack opening displacement as a function of the fraction of the maximum load at fatigue stages prior to, during and after overload at increasing distances behind the crack tip for the CG specimen.

3.3.2. Stress intensity factor range

It is widely believed that the decrease in SIF range is due to premature crack face contact, which means that only part of the loading range is applied to the crack. The SIF range estimated by the *J*-integral method (see Section 2.3) for the CG and NC specimens is shown in Fig. 9. In both cases the cracks are straight and perpendicular to the load such that the Mode II loading can be neglected. $\Delta a/r_p^{OL}$ represents the normalized crack length relative to the overload location with $\Delta a/$

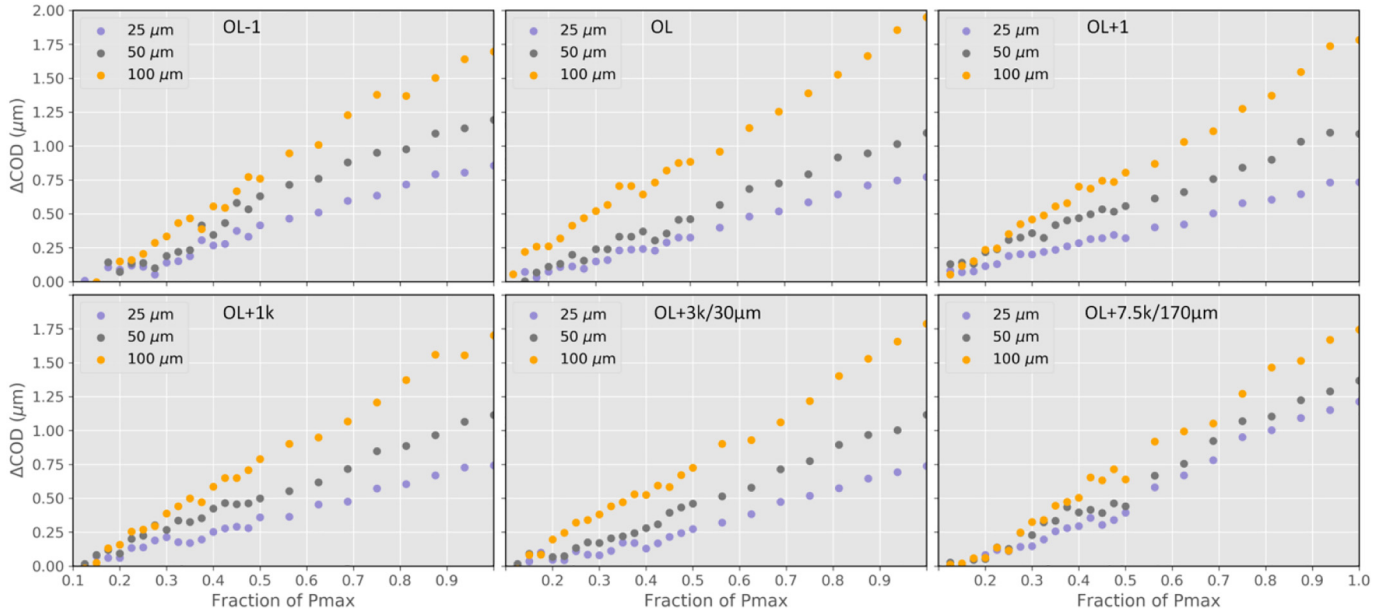

Fig. 8. Crack opening displacement as a function of the fraction of the maximum load at fatigue stages prior to, during and after overload at increasing distances behind the crack tip for the NC specimen.

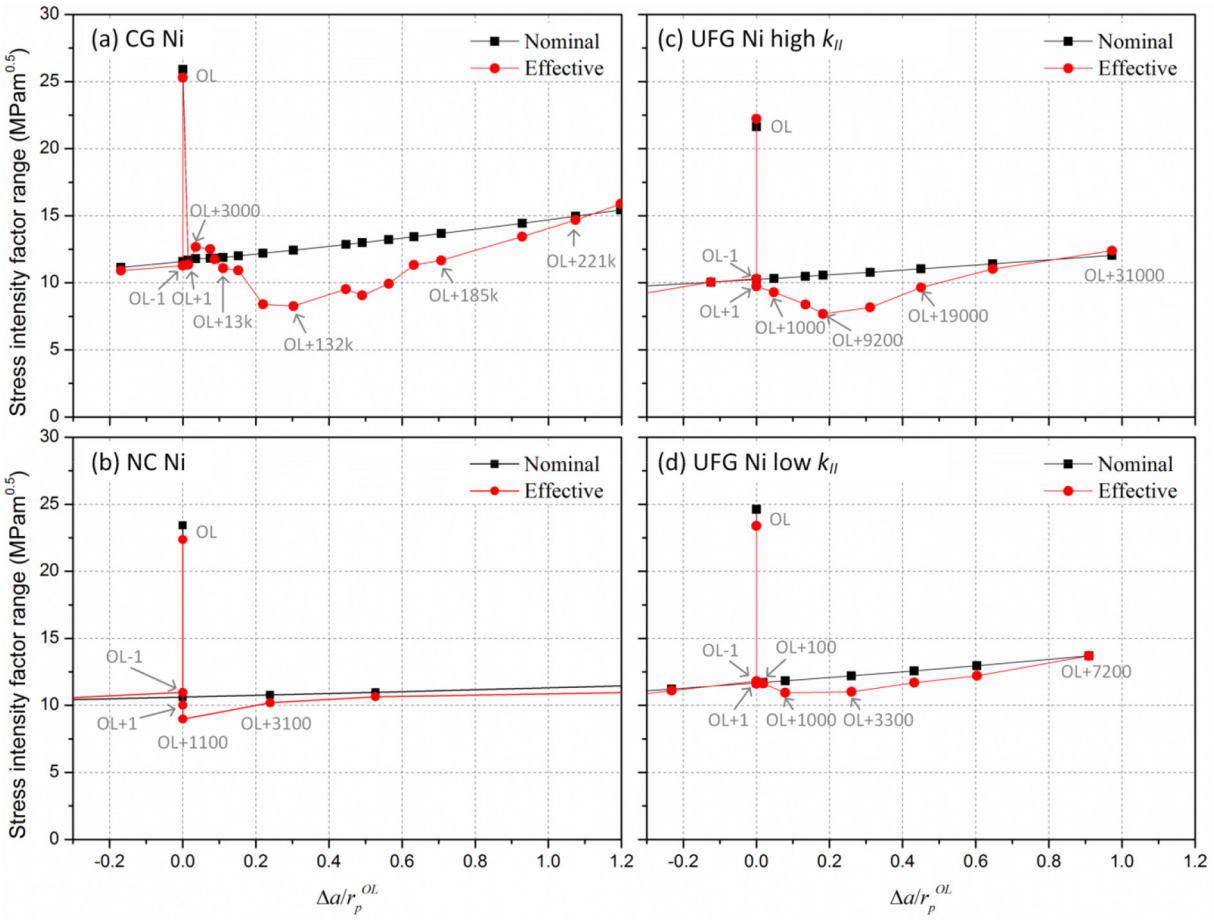

Fig. 9. Comparison between the nominal and effective (inferred from the crack-tip displacement field) SIF range prior to, at and after overload for (a) CG Ni, (b) NC Ni, (c) high k_{II} case of UFG Ni and (d) low k_{II} case of UFG Ni. Δa in the x-axis describes the relative distance from the overload position, with negative values indicating the distance before overload and positive values after overload. r_p^{OL} is the theoretically predicted forward overload plastic zone. The results for the UFG specimens are taken from [14].

$r_p^{OL} = 1$ indicating that the crack has grown through the overload plastic zone. The results for the UFG specimens are redrawn from the original data taken from [14] for comparison purposes. The overall SIF range for the high k_{II} case of UFG Ni is a little lower (10%) than for the other specimens due to the deflected crack path which reduces the local SIF range.

It is evident that overload has the longest range effect on the CG specimen in terms of the normalized crack length with a reduction in effective SIF range still being observed when $\Delta a/r_p^{OL} > 1$. The FCG rate retardation distance for the UFG specimens is smaller than r_p^{OL} while for the NC case the retardation effect is transient. A significant decrease in SIF range is observed for both the CG and the high k_{II} case of UFG specimens. This is reflected in the FCG results (in Fig. 4), which show a more dramatic reduction in crack growth rate.

For all cases, the SIF range does not drop immediately after overload, with this only occurring after the crack has grown somewhat further into the overload plastic zone (after ~1000 cycles). This is consistent with the ΔCOD and FCG results. Although residual stress cannot be measured by DIC, it is reasonable to infer that residual stress, which reduces both the mean stress experienced by the crack tip and the crack opening displacement, contributes to crack closure.

3.4. Fractography analysis

While crack closure has been measured by DIC for the CG specimen, it is still not clear whether the crack faces come into contact for the NC specimen. The SIF range results estimated from the displacement field suggest, at most, only slight and transient crack face contact. Neither the diffraction results nor the crack opening displacement results show evidence of crack closure. In order to find evidence of crack face contact, fractography was carried out on both specimens as shown in Figs. 10 and 11.

For NC Ni, the overload boundary (as observed for the UFG specimens [14]) is evident at low magnification (see Fig. 10a), though it is very narrow. The regions before and after overload are smooth. In the boundary region, crack face contact scars composed of clusters of grains are observed at high magnification (see Fig. 10b and c). It is not surprising that crack face contact through the mid-thickness (under plane strain) is not as significant as that near the surface (under plane stress). However, the largest contact distance (near the surface) is <10 μm, which means the closure effect is very weak and transient. This makes it difficult to detect by X-ray diffraction and DIC.

For the CG specimen, no clear boundary is observed at low magnification. Instead, a very rough fracture surface with many dark and flat facets indicating crack face contact locations is observed, as indicated in Fig. 11a. The images at high magnification (see Fig. 11b and c) depict crack face contact regions that only comprise several grains rather than a cluster of grains, as observed for the fine grained specimens, which is due to the very rugged and tortuous fracture surface. This is probably the reason for the disappearance of the overload boundary.

3.5. Surface roughness results

Crack face contact is observed for all the Ni specimens after the application of overload, which makes roughness-induced crack closure

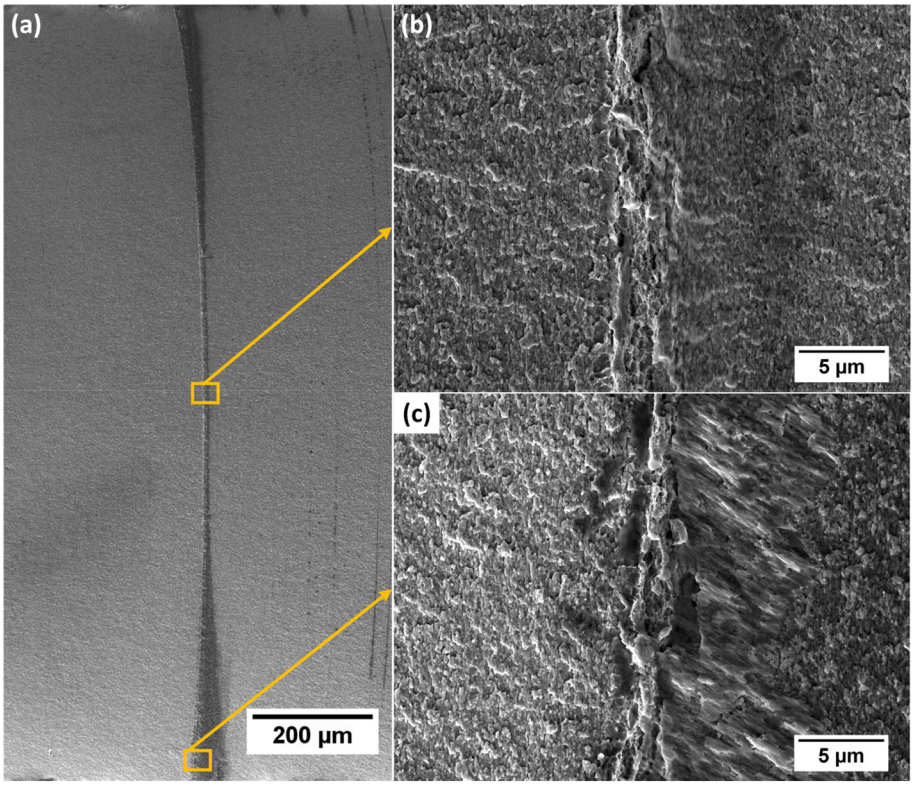

Fig. 10. Fractographs from the experiment for NC Ni. (a) Low magnification image of the full crack face. The boundary dividing the fractograph into two parts is the overload position. (b) High magnification through mid-thickness. (c) High magnification near the surface. The crack propagation direction is from left to right.

an important retardation mechanism in the post-overload regime. 3D roughness profiles extracted at the overload position through the mid-thickness for all the Ni specimens by a confocal laser scanner, NanoFocus μScan Custom, are shown in Fig. 12. For the NC and UFG specimens, an area of $200 \times 200\ \mu m^2$ was examined and the scale of the vertical axis was set the same. However, a larger area of

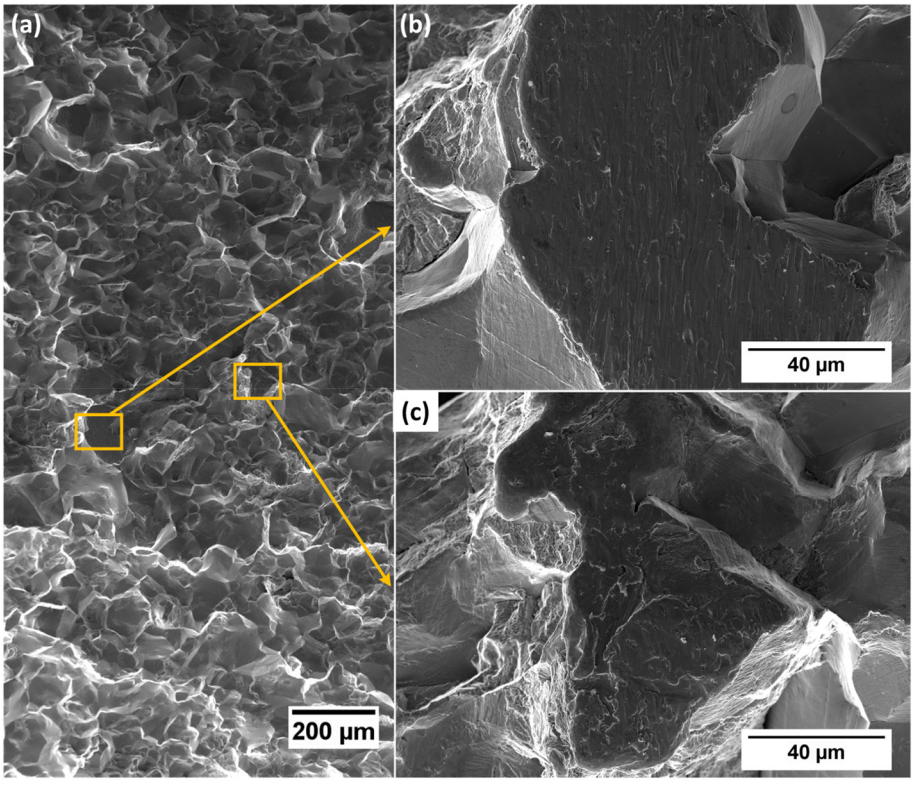

Fig. 11. Fractographs from the experiment for CG Ni. (a) Low magnification image of full crack face. (b, c) High magnification showing flat and dark regions where discontinuous crack closure takes place.

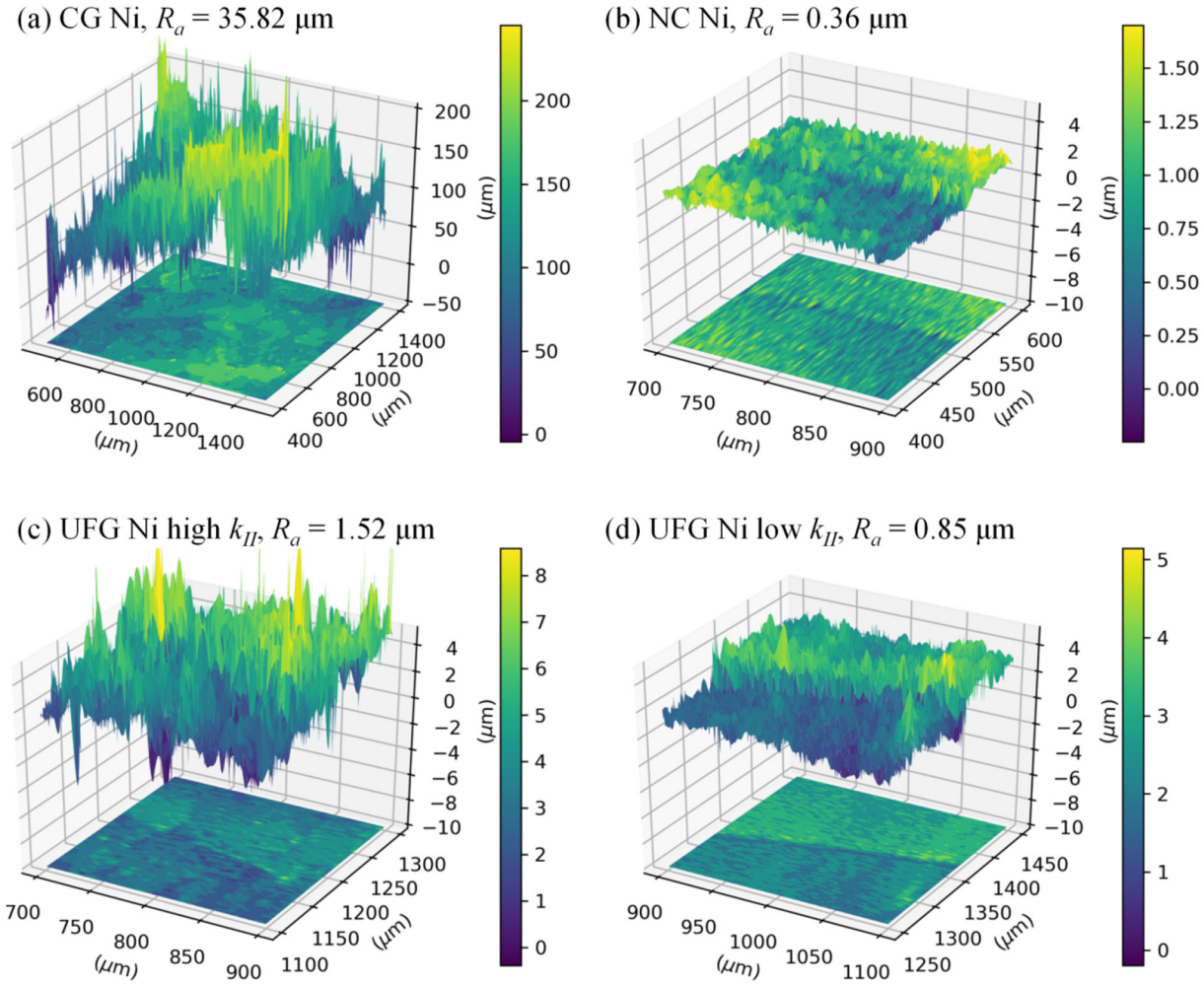

Fig. 12. 3D roughness profiles extracted at the overload position for (a) CG Ni, (b) NC Ni, (c) high k_{II} case of UFG Ni and (d) low k_{II} case of UFG Ni. The results for the UFG specimens are taken from [14].

$1000 \times 1000\ \mu m^2$ was interrogated and the vertical axis was scaled to a larger range for the CG specimen because of its significantly larger grain size and hence rougher fracture surface.

The overload boundary is observed in the 2D contour map below the 3D profile for the NC and UFG cases while it is absent for the CG specimen, which is in agreement with the fractography observations (in Section 3.4). The NC specimen has the smallest roughness value due to its smallest grain size. Followed by is the low k_{II} case of UFG Ni with the crack propagating along the grain elongation direction. Compared with the high k_{II} case of the UFG specimen of the same grain size with the crack growing approximately perpendicular to the grain elongation direction, the relatively straight and flat crack morphology for the low k_{II} case of UFG Ni leads to a smaller surface roughness value. The roughness value for CG Ni is considerably larger than the others because of its large grains.

4. Discussion

4.1. Delayed crack growth retardation

The FCG rates (shown in Fig. 4) for all the Ni specimens, except NC Ni, are not retarded immediately after overload. Instead, they remain largely the same as the baseline state for a specific number of cycles. In some cases, a transient acceleration in FCG rate has even been observed [43–47]. As the crack propagates into the overload plastic zone, the FCG rate gradually declines. It should be noted that the detectability of the transient phenomenon immediately after overload highly depends on the accuracy of the crack length measurement techniques. The enlarged plastic zone induced by overload can also add uncertainties to the determination of the crack length on the sample surface. For the NC specimen, FCG retardation only lasts for several tens of microns. It is therefore difficult for the DIC camera to capture a detailed variation in FCG rate. The limited retardation distance and severity suggest that the overload does not have a significant effect on the NC specimen. For the other specimens, the overload plastic zone is much larger than for the NC case and therefore the variation in FCG rate within the retardation zone induced by overload is recorded in detail.

The post-mortem crack morphology for all the specimens is shown in Fig. 13a. For the CG and UFG specimens, the crack flanks that are significantly opened by the overload come into contact after overload. The crack opening becomes increasingly larger as the crack propagates further away from the overload position. This is schematically illustrated in Fig. 13b. The forward plastic zone, which is small during baseline fatigue in stage (i), is enlarged by the overload event in stage (ii). The crack tip is also blunted by the overload. Due to the morphological misfit between the plastically stretched material around the crack tip and the rest of the elastically deformed material during unloading, a compressive zone is then developed ahead of the crack tip. This can be inferred from the energy dispersive X-ray diffraction results on NC Ni in terms of the decrease in peak stress after overload (see Figs. 5 and 6). The

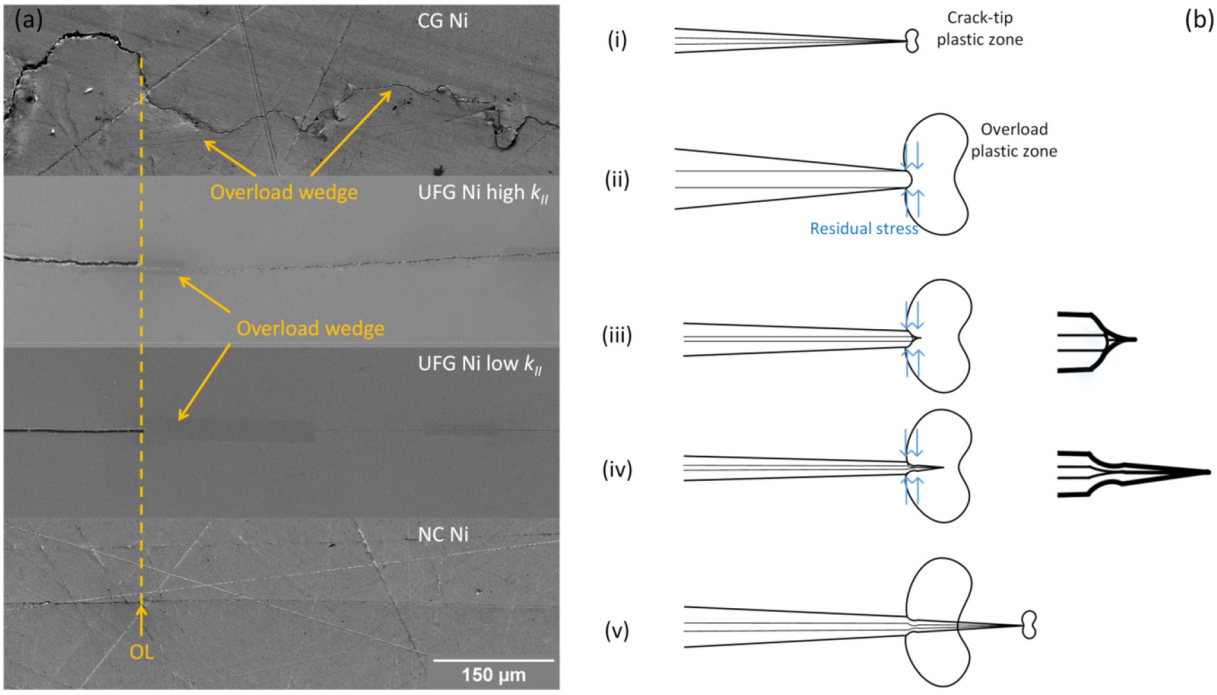

Fig. 13. (a) Post-mortem crack morphology for the Ni specimens showing crack face contact within a short distance immediately after overload as a wedge that holds the rest of the crack open except for NC Ni. (b) Schematic illustrating the development of the overload wedge. The thick lines represent the crack flanks at P_{max} and the thin lines represent the crack flanks at P_{min}.

residual compressive stress was also captured by monochromatic synchrotron X-ray diffraction on the UFG specimens in [14]. Though the crack flanks are getting closer during unloading, no crack face contact is observed behind the crack tip. This is evidenced by both the fractography results, which show that overload-induced crack closure starts to take shape after the application of overload, and the DIC results (see Fig. 9), which demonstrate that the effective ΔK does not drop immediately after overload. It is likely that the retardation effects of residual stress and crack-tip blunting caused by overload are offset by the sudden increase in the external load and the absence of crack closure brought about by the crack opening. Therefore, the FCG rates do not decrease immediately after overload, as indicated in Fig. 4. As the crack initiates from the blunted crack tip and propagates a short distance into the overload plastic zone under the influence of the overload-induced residual stress (indicated in stage (iii)), crack face contact occurs at P_{min} and becomes more and more significant, which also strengthens the effect of roughness-induced crack closure. At this stage, the SIF range and the mean stress are reduced by crack closure and residual stress. This brings the FCG rate down to its smallest value. As the crack grows further into the overload plastic zone in stage (iv), the crack opening immediately behind the crack tip gradually increases because of the increasingly applied SIF range as the crack propagates. When the crack grows out of the retardation zone in stage (v), neither crack closure nor residual stress can act. Therefore, the FCG rate recovers to the baseline state.

It is noteworthy that the overload retardation zone for CG Ni is slightly larger than its overload plastic zone, whereas for NC Ni the retardation distance is much smaller than the corresponding overload plastic zone (see Fig. 9). Due to the very high strength of the NC specimen, overload cannot generate a large enough plastic stretch meaning that plasticity-induced crack closure and residual stress effects are largely suppressed.

4.2. The effect of grain size

Although similar loading conditions are applied to the specimens having different grain sizes, different degrees of crack growth retardation are observed (see Fig. 4). Various retardation mechanisms including plasticity-induced crack closure, residual stress, crack path tortuosity and roughness-induced crack closure have been considered to explain the difference. However, grain size is one of the primary causes for the difference of the retardation mechanisms.

A smaller grain size can lead to higher strength and hence smaller plastic zone. In other words, the material becomes harder to deform due to the reduced grain size, which reduces the shape misfit between the plastically stretched and the elastically deformed material. Therefore, the primary retardation mechanisms (plasticity-induced crack closure and residual stress) are minimised, which is supported by the FCG results (see Fig. 4) and the SIF results (see Fig. 9).

Furthermore, grain refinement not only increases the strength of the material but also reduces the tortuosity of the crack path (see Fig. 13a) and the roughness of the fractured surface (see Fig. 12). Crack deflection can reduce the effective SIF and increase the local Mode II SIF [15]. The Mode II component leads to the relative movement of the crack surfaces along the crack propagation direction and hence strengthens the effect of roughness-induced crack closure at low external loading levels. Though these are not the primary retardation mechanisms, they can play an important role when the FCG is significantly reduced. Consequently, the NC specimen has the smallest grain size and is found to be least affected by the retardation mechanisms.

This paper systematically outlines the effect of grain refinement on crack growth and sheds new light on the design of new materials, such as gradient metallic materials with gradients in grain size ranging from nanometres to microns [48–50]. The nano layer provides high strength and resistance to crack initiation and wear while the coarse-grain layer contributes to high ductility and resistance to crack propagation. Overall this kind of hierarchical structure might be expected to show superior combination of high strength and toughness compared to single grain-sized materials.

4.3. Further observations

The effective crack driving force can not only be derived from the crack-tip displacement field by the *J*-integral method (see Section 2.3),

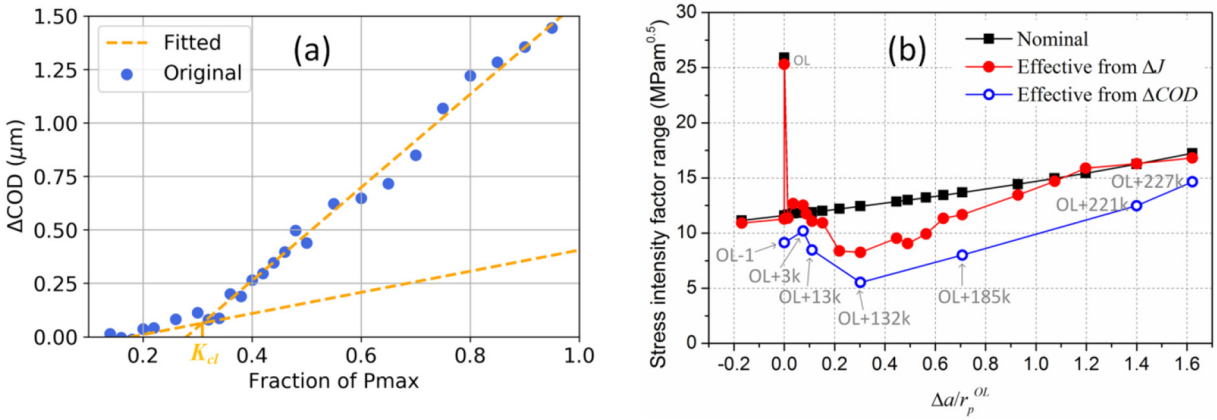

Fig. 14. (a) Inferring the closure stress intensity factor, K_{cl}, at which the crack faces start to contact from the Δ*COD* results (as shown in Figs. 7 and 8). (b) Comparison between the effective stress intensity factor ranges determined from the Δ*J* and Δ*COD* results for CG Ni.

it can also be determined from the Δ*COD* results (see Figs. 7 and 8). This approach is similar to the compliance technique by using mechanical strain or displacement gauges [51]. In order to obtain a relatively accurate estimation of K_{cl}, which is the stress intensity factor where the crack starts to close, the data points on both sides of the 'closure knee' are linearly fitted respectively (as shown in Fig. 14a). The fraction of P_{max} at the intersection of the two fitted lines represents crack closure starts to occur, from which K_{cl} and therefore the effective SIF range, ΔK^{eff}, can be determined as follows.

$$\Delta K^{eff} = K^{eff}_{\max} - K_{cl} \tag{6}$$

The results are shown in Fig. 14b comparing the effective SIF range evaluated by the *J*-integral and the compliance methods. It is observed that the values assessed from the Δ*COD* curves are well below the nominal and the Δ*J* estimated ones. Theoretically, the effective crack driving force should be determined by

$$\Delta K^{eff} = K^{eff}_{\max} - K^{eff}_{\min} \tag{7}$$

The effective SIF is still decreasing as the specimen is unloaded from K_{cl} to the minimum load because the crack does not fully close at K_{cl}. This means Eq. (6) actually underestimates ΔK^{eff}. The ΔK^{eff} values determined by Eq. (6) will be more significantly underestimated if the closure effect is prominent (e.g. OL+132k in Figs. 14b and 7), which means $K^{eff}_{\min}$ at this moment is evidently smaller than K_{cl}.

The parts of the cyclic loading from K_{cl} to $K^{eff}_{\min}$ and from $K^{eff}_{\min}$ to K_{cl} could have a contribution to the cyclic deformation and therefore the crack growth. Eq. (6) could be used if closure is not significant when K_{cl} is close to $K^{eff}_{\min}$. However, Eq. (7) gives a more accurate estimation of ΔK^{eff}, which can be achieved by fitting the displacement or strain field through least square method [14] or by the *J*-integral method.

Another interesting finding is in Fig. 9 showing that the retardation distance for CG Ni is slightly larger than its monotonic plastic zone induced by overload while the retardation length for NC Ni is significantly smaller than its overload forward plastic zone. This might be explained by cyclic softening observed in UFG Ni [52] and NC Ni [53] due to grain coarsening especially under high strains or stresses. Plasticity-induced closure is due to the synergetic effect of the monotonic and cyclic plastic deformation around the crack tip. The forward deformation increases while the reverse deformation decreases the closure load and thus the closure effect. The reverse deformation becomes more pronounced for the NC and UFG cases due to cyclic softening especially after overload. Therefore, the closure effect becomes smaller for cyclic softening materials compared to hardening materials in terms of the relative retardation distance to the overload plastic zone.

5. Conclusion

Fatigue experiments under constant amplitude loading at a stress ratio of $R = 0.1$ were conducted on two compact tension specimens of nanocrystalline and coarse grained Ni. A 100% overload ($P_{OL} = 2P_{max}$) was applied generating overload forward plastic zone sizes (estimated by Irwin's model) of 120 μm and 1440 μm, respectively. Energy dispersive X-ray diffraction measurements were conducted on the NC specimen to study the variation in stress as a function of crack growth past the overload. Digital image correlation was applied for both cases to measure the crack length, crack opening displacement and the stress intensity factor range. Post-mortem fractography analysis and fracture surface roughness measurements were conducted to help understand the retardation mechanisms. The results are compared with our previous study on ultra-fine grained Ni under the same loading conditions; this research therefore covers grain sizes ranging from microns down to nanometers.

It can be concluded that:

(1) FCG retardation was observed for all the specimens after the application of overload. CG Ni shows the sharpest decrease in FCG rate and the longest retardation distance while only transient retardation was observed for NC Ni. Due to the very small plastic zone, flat and smooth crack surfaces and straight crack path for the NC specimen, it is least affected by overload.

(2) For the CG and UFG specimens that were evidently retarded by the overload, no significant decrease in FCG was observed immediately after overload. It is believed that the sudden rise in applied load and the significant crack opening caused by overload impede crack closure and offset the retardation effects of crack-tip blunting and residual stress. As the crack grows further into the overload plastic zone, an overload wedge is developed due to the combined effects of plasticity-induced crack closure and residual stress that retard crack propagation.

(3) Grain size plays a fundamental role in the fatigue overload behaviour of the material. Grain refinement that strengthens the material reduces the plasticity that is introduced by the overload. The primary retardation mechanisms, plasticity-induced crack closure and residual stress, are weakened. Due to smaller grain size, the crack surfaces get less rough and the crack becomes straighter, which also diminishes the retardation effects of crack tortuosity and roughness-induced crack closure.

Data availability

The raw data and processed data required to reproduce these findings are available upon request.

CRediT authorship contribution statement

Wen Zhang: Conceptualization, Methodology, Formal analysis, Writing - original draft, Writing - review & editing. **Christopher A. Simpson:** Software, Investigation, Writing - review & editing. **Pablo Lopez-Crespo:** Investigation, Writing - review & editing. **Mehdi Mokhtarishirazabad:** Investigation, Writing - review & editing. **Thomas Buslaps:** Investigation, Writing - review & editing. **Reinhard Pippan:** Resources, Writing - review & editing. **Philip J. Withers:** Conceptualization, Writing - review & editing, Supervision, Funding acquisition.

Declaration of competing interest

The authors declare that they have no known competing financial interests or personal relationships that could have appeared to influence the work reported in this paper.

Acknowledgement

We acknowledge the ESRF for time at beamline ID15A under proposal MA-3405; we acknowledge Diamond Light Source for time at beamline I12-JEEP under proposal EE16647 for the UFG experiment. WZ is grateful for the financial support from the China Scholarship Council (CSC). PJW acknowledges support from the European Research Council grant No. 695638 CORREL-CT. Financial support from Programa Opeativo FEDER (Junta de Andalucia, Spain) through grant reference UMA18-FEDERJA-250, from Ministerio de Economía y Competitividad through grant reference MAT2016-76951-C2-2-P and from Ministerio de Educación, Cultura y Deporte through mobility grant Jose Castillejo for PLC to visit the University of Manchester in 2017 are also acknowledged.

Appendix A

It can be seen from Eq. (3) that if the strain and stress matrices of each element on the integral path and the relative distance between elements are determined, the *J*-integral through a specific contour path can then be estimated. A routine was written in Python and can be directly performed to the crack-tip displacement field to calculate the *J*-integral. Here the evaluation procedure and the verification of the routine are introduced.

A.1. Estimation of the displacement field

As is described in Section 2.3, the displacement field in the crack opening direction (u_{yy}) and along the crack propagation direction (u_{xx}) is estimated using the commercial software LaVision DaVis ver.8.4. Therefore, the displacement matrices in both directions are obtained as shown in Fig. 3.

A.2. Estimation of the strain field

Although the strain field can be directly calculated using specific algorithms or numerical differentiation of the displacement field, the great variation in the strain results due to the noise of the estimated displacement results indicates that these methods cannot be used for reliable strain measurement [54,55]. Therefore, it is widely believed that smoothing the displacement field first followed by differentiation would improve the accuracy of the strain measurement [56].

In order to calculate the full-field strain distribution, a small strain calculation window consisting of $(2\,m+1)\times(2\,m+1)$ points is first defined as shown in Fig. A.1. The strain calculation window should be small enough to ensure the estimated results can accurately describe the local deformation. However, the calculation window cannot be too small such that the noise can be effectively reduced. After an appropriate strain calculation window size is selected, the displacement vectors within it can be approximated to a linear plane:

$$\begin{aligned} u_{xx}(i,j) &= a_0 + a_1 x + a_2 y \\ u_{yy}(i,j) &= b_0 + b_1 x + b_2 y \end{aligned} \qquad (i,j = -m:m) \tag{A.1}$$

Eq. (A.1) can be rewritten into the form of matrix as

$$\begin{pmatrix} 1 & -m & -m \\ 1 & -m+1 & -m \\ \vdots & \vdots & \vdots \\ 1 & 0 & 0 \\ \vdots & \vdots & \vdots \\ 1 & m-1 & m \\ 1 & m & m \end{pmatrix} \begin{pmatrix} a_0 \\ a_1 \\ a_2 \end{pmatrix} = \begin{pmatrix} u_{xx}(-m,-m) \\ u_{xx}(-m+1,-m) \\ \vdots \\ u_{xx}(0,0) \\ \vdots \\ u_{xx}(m-1,m) \\ u_{xx}(m,m) \end{pmatrix} \tag{A.2}$$

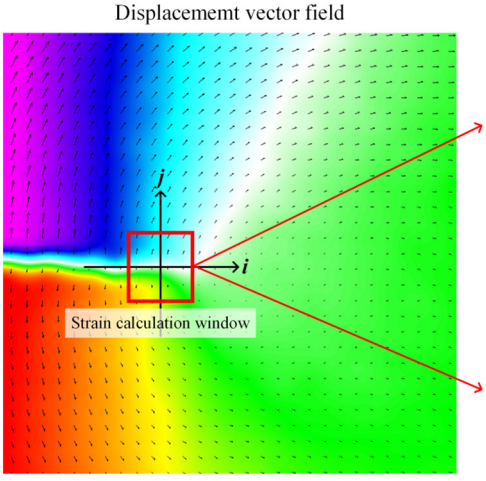

Local u_{yy}-displacememt field

u_{yy}(-m,m)	…	u_{yy}(0,m)	…	u_{yy}(m,m)
…	…	…	…	…
u_{yy}(-m,0)	…	u_{yy}(0,0)	…	u_{yy}(m,0)
…	…	…	…	…
u_{yy}(-m,-m)	…	u_{yy}(0,-m)	…	u_{yy}(m,-m)

Local u_{xx}-displacememt field

u_{xx}(-m,m)	…	u_{xx}(0,m)	…	u_{xx}(m,m)
…	…	…	…	…
u_{xx}(-m,0)	…	u_{xx}(0,0)	…	u_{xx}(m,0)
…	…	…	…	…
u_{xx}(-m,-m)	…	u_{xx}(0,-m)	…	u_{xx}(m,-m)

Fig. A.1. Schematic showing the principle of the pointwise least squares algorithm for full-field strain calculation. The red box represents the strain calculation window comprising $(2\,m+1)\times(2\,m+1)$ points of the displacement field in the two directions (u_{yy} and u_{xx}).

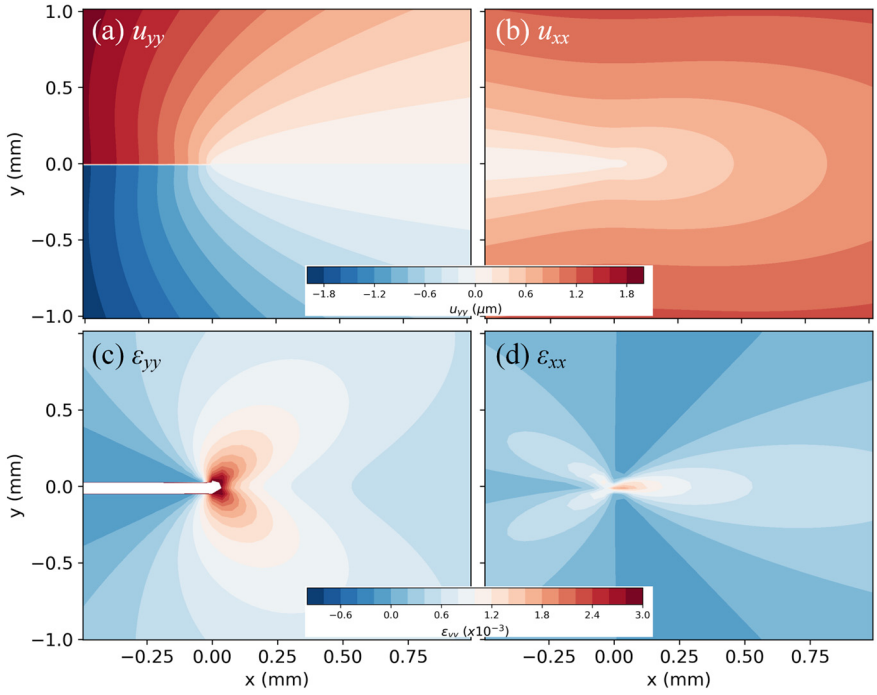

Fig. A.2. Theoretically generated displacement fields (a) in the crack opening direction and (b) along the crack growth direction. Strain fields calculated by the least squares method (c) in the crack opening direction and (d) along the crack growth direction.

$$\begin{pmatrix} 1 & -m & -m \\ 1 & -m+1 & -m \\ \vdots & \vdots & \vdots \\ 1 & 0 & 0 \\ \vdots & \vdots & \vdots \\ 1 & m-1 & m \\ 1 & m & m \end{pmatrix} \begin{pmatrix} b_0 \\ b_1 \\ b_2 \end{pmatrix} = \begin{pmatrix} u_{yy}(-m,-m) \\ u_{yy}(-m+1,-m) \\ \vdots \\ u_{yy}(0,0) \\ \vdots \\ u_{yy}(m-1,m) \\ u_{yy}(m,m) \end{pmatrix} \tag{A.3}$$

Thus the coefficients in Eq. (A.1) can be determined by the least squares method. a_1 and b_2 are the normal strains while a_2 and b_1 are the components of shear strains.

A.3. Estimation of the stress field

Once the strain matrix is determined, the stress matrix can be evaluated by

$$\{\sigma\} = [D]\{\varepsilon\} \tag{A.4}$$

where D is the stress-strain matrix. Here for linear elastic materials under plane stress conditions, Eq. (A.4) can be rewritten as

$$\begin{pmatrix} \sigma_{xx} \\ \sigma_{yy} \\ \sigma_{xy} \end{pmatrix} = \frac{E}{1-\nu^2} \begin{pmatrix} 1 & \nu & 0 \\ \nu & 1 & 0 \\ 0 & 0 & (1-\nu)/2 \end{pmatrix} \begin{pmatrix} \varepsilon_{xx} \\ \varepsilon_{yy} \\ \varepsilon_{xy} \end{pmatrix} \tag{A.5}$$

where E is the elastic modulus and ν is the Poisson's ratio.

Therefore, with the input of the displacement fields (u_{xx} and u_{yy}) and the material properties (E and ν), the routine can be implemented to calculate the J integral, which is the sum of the value of each element on any user defined contours as shown in Fig. 3.

A.4. Verification

In order to verify the routine, a perfect displacement field in two orientations (u_{yy} and u_{xx}) was first generated as shown in Fig. A.2(a and b). The applied stress intensity factor, K_I, is equal to 10 MPam$^{0.5}$, with Young's Modulus $E = 193.3$ GPa and Poisson's ratio $\nu = 0.33$, which are the bulk properties of nickel following the Kroner Modelling Scheme [32]. Theoretically, the J-integral should be path-independent for any contour surrounding the crack tip in the elastic regime. This means, in this case, the routine should give a value that is very close to 10 MPam$^{0.5}$ no matter which integration path is selected or how large the strain calculation window is.

The nominal strain fields calculated by the least squares method discussed in Section A.2 are shown in Fig. A.2(c and d). Four integration paths (as shown in Fig. 3) and three strain calculation windows (indicated by m) were considered for the comparison of J. The J values were then converted to K_I by Eq. (4). The corresponding results are given in Table A.1 and are in good agreement with the applied value.

Therefore, this routine for determining the J-integral is reliable and computationally efficient. Accurate determination of the crack-tip position is not required. As long as the displacement fields are obtained, the J values can be quickly estimated with the known input variables E and ν. A small integration contour with small strain calculation window gives higher accuracy and hence is suggested for the J estimation.

Table A.1
J-integral results (converted to K_I in MPa m$^{0.5}$) estimated by the routine for various integration contours and strain calculation windows. The theoretically applied K_I is 10 MPam$^{0.5}$.

	$m = 1$	$m = 3$	$m = 5$
Path 1	9.84	9.78	9.19
Path 2	9.39	9.30	9.10
Path 3	9.22	9.15	9.07
Path 4	9.14	9.09	9.06

References

[1] W.N. Findley, A theory for the effect of mean stress on fatigue of metals under combined torsion and axial load or bending, J. Eng. Ind. 81 (1959) 301–305, https://doi.org/10.1115/1.4008327.
[2] K. Walker, The effect of stress ratio during crack propagation and fatigue for 2024-T3 and 7075-T6 aluminum, Eff. Environ. Complex Load Hist. Fatigue Life, ASTM

International, 100 Barr Harbor Drive, PO Box C700, West Conshohocken, PA 19428-2959, 1970https://doi.org/10.1520/STP32032S , (pp. 1-1–14).
[3] N.E. Dowling, C.A. Calhoun, A. Arcari, Mean stress effects in stress-life fatigue and the Walker equation, Fatigue Fract. Eng. Mater. Struct. 32 (2009) 163–179, https://doi.org/10.1111/j.1460-2695.2008.01322.x.
[4] W. Elber, The significance of fatigue crack closure, Damage Toler. Aircr. Struct, ASTM International, West Conshohocken, PA 1971, pp. 230–242, https://doi.org/10.1520/STP26680S.
[5] E. Wolf, Fatigue crack closure under cyclic tension, Eng. Fract. Mech. 2 (1970) 37–45, https://doi.org/10.1016/0013-7944(70)90028-7.
[6] A.K. Vasudeven, K. Sadananda, N. Louat, A review of crack closure, fatigue crack threshold and related phenomena, Mater. Sci. Eng. A 188 (1994) 1–22, https://doi.org/10.1016/0921-5093(94)90351-4.
[7] J. Schijve, Fatigue crack closure: observations and technical significance, in: J. Newman, W. Elber (Eds.), Mech. Fatigue Crack Clos, ASTM International, West Conshohocken, PA 1988, pp. 5–34, https://doi.org/10.1520/STP27198S.
[8] R.O. Ritchie, Mechanisms of fatigue crack propagation in metals, ceramics and composites: role of crack tip shielding, Mater. Sci. Eng. A 103 (1988) 15–28, https://doi.org/10.1016/0025-5416(88)90547-2.
[9] R. Pippan, A. Hohenwarter, Fatigue crack closure: a review of the physical phenomena, Fatigue Fract. Eng. Mater. Struct. 40 (2017) 471–495, https://doi.org/10.1111/ffe.12578.
[10] M.D. Sangid, G.J. Pataky, H. Sehitoglu, R.F. Hamilton, H.J. Maier, High resolution analysis of opening and sliding in fatigue crack growth, Int. J. Fatigue 37 (2012) 134–145, https://doi.org/10.1016/j.ijfatigue.2011.11.001.
[11] P.J. Withers, Residual stress and its role in failure, Reports Prog. Phys. 70 (2007) 2211–2264, https://doi.org/10.1088/0034-4885/70/12/R04.
[12] A. Steuwer, M. Rahman, A. Shterenlikht, M.E. Fitzpatrick, L. Edwards, P.J. Withers, The evolution of crack-tip stresses during a fatigue overload event, Acta Mater. 58 (2010) 4039–4052, https://doi.org/10.1016/j.actamat.2010.03.013.
[13] C.A. Simpson, S. Kozuki, P. Lopez-Crespo, M. Mostafavi, T. Connolley, P.J. Withers, Quantifying fatigue overload retardation mechanisms by energy dispersive X-ray diffraction, J. Mech. Phys. Solids. 124 (2019) 392–410, https://doi.org/10.1016/j.jmps.2018.10.020.
[14] W. Zhang, C.A. Simpson, T. Leitner, X. Zhang, R. Pippan, P.J. Withers, The effect of anisotropic microstructure on the crack growth and fatigue overload behaviour of ultrafine-grained nickel, Acta Mater. 184 (2020) 225–240, https://doi.org/10.1016/j.actamat.2019.11.024.
[15] S. Suresh, Fatigue crack deflection and fracture surface contact: micromechanical models, Metall. Trans. A. 16 (1985) 249–260, https://doi.org/10.1007/BF02816051.
[16] T. Hanlon, E.D. Tabachnikova, S. Suresh, Fatigue behavior of nanocrystalline metals and alloys, Int. J. Fatigue 27 (2005) 1147–1158, https://doi.org/10.1016/j.ijfatigue.2005.06.035.
[17] R. Valiev, Nanostructuring of metals by severe plastic deformation for advanced properties, Nat. Mater. 3 (2004) 511–516, https://doi.org/10.1038/nmat1180.
[18] T. Leitner, A. Hohenwarter, R. Pippan, Revisiting fatigue crack growth in various grain size regimes of Ni, Mater. Sci. Eng. A 646 (2015) 294–305, https://doi.org/10.1016/j.msea.2015.08.071.
[19] A. Hohenwarter, R. Pippan, Fracture and fracture toughness of nanopolycrystalline metals produced by severe plastic deformation, Phil. Trans. R. Soc. A 373 (2015) 20140366, https://doi.org/10.1098/rsta.2014.0366.
[20] S. Suresh, R.O. Ritchie, A geometric model for fatigue crack closure induced by fracture surface roughness, Metall. Trans. A. 13 (1982) 1627–1631, https://doi.org/10.1007/BF02644803.
[21] G.T. Gray, J.C. Williams, A.W. Thompson, Roughness-induced crack closure: an explanation for microstructurally sensitive fatigue crack growth, Metall. Trans. A. 14 (1983) 421–433, https://doi.org/10.1007/BF02644220.
[22] R.O. Ritchie, S. Suresh, Some considerations on fatigue crack closure at near-threshold stress intensities due to fracture surface morphology, Metall. Trans. A. 13 (1982) 937–940, https://doi.org/10.1007/BF02642409.
[23] R. Pippan, G. Strobl, H. Kreuzer, C. Motz, Asymmetric crack wake plasticity – a reason for roughness induced crack closure, Acta Mater. 52 (2004) 4493–4502, https://doi.org/10.1016/j.actamat.2004.06.014.
[24] T.C. Lowe, Y.T. Zhu, Commercialization of nanostructured metals produced by severe plastic deformation processing, Adv. Eng. Mater. 5 (2003) 373–378, https://doi.org/10.1002/adem.200310076.
[25] M.A. Meyers, A. Mishra, D.J. Benson, Mechanical properties of nanocrystalline materials, Prog. Mater. Sci. 51 (2006) 427–556, https://doi.org/10.1016/j.pmatsci.2005.08.003.
[26] M.D. Sangid, G.J. Pataky, H. Sehitoglu, R.G. Rateick, T. Niendorf, H.J. Maier, Superior fatigue crack growth resistance, irreversibility, and fatigue crack growth–microstructure relationship of nanocrystalline alloys, Acta Mater. 59 (2011) 7340–7355, https://doi.org/10.1016/j.actamat.2011.07.058.
[27] P. Zhou, J. Zhou, Z. Ye, X. Hong, H. Huang, W. Xu, Effect of grain size and misorientation angle on fatigue crack growth of nanocrystalline materials, Mater. Sci. Eng. A 663 (2016) 1–7, https://doi.org/10.1016/j.msea.2016.03.105.
[28] W.S. LePage, A. Ahadi, W.C. Lenthe, Q.-P. Sun, T.M. Pollock, J.A. Shaw, S.H. Daly, Grain size effects on NiTi shape memory alloy fatigue crack growth, J. Mater. Res. 33 (2018) 91–107, https://doi.org/10.1557/jmr.2017.395.
[29] N.A. Fleck, Influence of stress state on crack growth retardation, in: J. Fong, R. Wei, R. Fields, R. Gangloff (Eds.), Basic Quest. Fatigue Vol. I, ASTM International, 100 Barr Harbor Drive, PO Box C700, West Conshohocken, PA 19428–2959, 1988https://doi.org/10.1520/STP23215S , (pp. 157-157–27).
[30] T.L. Anderson, FRACTURE MECHANICS Fundamentals and Applications, CRC Press, 2017https://doi.org/10.1201/9781315370293.
[31] P.J. Withers, M. Preuss, A. Steuwer, J.W.L. Pang, Methods for obtaining the strain-free lattice parameter when using diffraction to determine residual stress, J. Appl. Crystallogr. 40 (2007) 891–904, https://doi.org/10.1107/S0021889807030269.
[32] M.T. Hutchings, P.J. Withers, T.M. Holden, T. Lorentzen, Introduction to the Characterization of Residual Stress by Neutron Diffraction, CRC press, 2005.
[33] T.M. Holden, A.P. Clarke, R.A. Holt, Neutron diffraction measurements of intergranular strains in MONEL-400, Metall. Mater. Trans. A. 28 (1997) 2565–2576, https://doi.org/10.1007/s11661-997-0014-9.
[34] C.A. Simpson, Casimp/Pyxe: XRD Strain Analysis (Version v0.9.3), Zenodo, 2019https://doi.org/10.5281/zenodo.3381279.
[35] J.A. Begley, J.D. Landes, The J integral as a fracture criterion, in: H. Corten (Ed.), Fract. Toughness Part II, ASTM International, West Conshohocken, PA 1972, pp. 1–23, https://doi.org/10.1520/STP38816S.
[36] ASTM E647-15e1 Standard Test Method for Measurement of Fatigue Crack Growth Rates. , ASTM International, West Conshohocken, PA, 2015https://doi.org/10.1520/E0647-15E01.
[37] ASTM International, ASTM E399–17 Standard Test Method for Linear-Elastic Plane-Strain Fracture Toughness KIc of Metallic Materials, ASTM International, West Conshohocken, PA, 2017https://doi.org/10.1520/E0399-17.
[38] W. Zhang, C.A. Simpson, R. Pippan, P.J. Withers, The Effect of R Ratio on Fatigue Overload Behaviour of Ultrafine-Grained Nickel, 2020 (in preparation).
[39] P.F.P. de Matos, D. Nowell, Numerical simulation of plasticity-induced fatigue crack closure with emphasis on the crack growth scheme: 2D and 3D analyses, Eng. Fract. Mech. 75 (2008) 2087–2114, https://doi.org/10.1016/j.engfracmech.2007.10.017.
[40] E. von Euw, R. Hertzberg, R. Roberts, Delay effects in fatigue crack propagation, Stress Anal. Growth Cracks Proc. 1971 Natl. Symp. Fract. Mech. Part 1, ASTM International, West Conshohocken, PA, 1996https://doi.org/10.1520/STP34123S , (pp. 230-230–30).
[41] P.J. Bernard, T.C. Lindley, C.E. Richards, The effect of single overloads on fatigue-crack propagation in steels, Met. Sci. 11 (1977) 390–398, https://doi.org/10.1179/msc.1977.11.8-9.390.
[42] L.P. Borrego, J.M. Ferreira, J.M. Pinho da Cruz, J.M. Costa, Evaluation of overload effects on fatigue crack growth and closure, Eng. Fract. Mech. 70 (2003) 1379–1397, https://doi.org/10.1016/S0013-7944(02)00119-4.
[43] C.S. Shin, N.A. Fleck, Overload retardation in a structural steel, Fatigue Fract. Eng. Mater. Struct. 9 (1987) 379–393, https://doi.org/10.1111/j.1460-2695.1987.tb00464.x.
[44] C. Ward-Close, R. Ritchie, On the role of crack closure mechanisms in influencing fatigue crack growth following tensile overloads in a titanium alloy: near threshold versus higher Δ, Mech. Fatigue Crack Clos. ASTM International, 100 Barr Harbor Drive, PO Box C700, West Conshohocken, PA 19428-2959, 2009https://doi.org/10.1520/STP27202S , (pp. 93-93–19).
[45] C.M. Ward-Close, A.F. Blom, R.O. Ritchie, Mechanisms associated with transient fatigue crack growth under variable-amplitude loading: an experimental and numerical study, Eng. Fract. Mech. 32 (1989) 613–638, https://doi.org/10.1016/0013-7944(89)90195-1.
[46] C. Shin, S. Hsu, On the mechanisms and behaviour of overload retardation in AISI 304 stainless steel, Int. J. Fatigue 15 (1993) 181–192, https://doi.org/10.1016/0142-1123(93)90175-P.
[47] C. Bichler, R. Pippan, Effect of single overloads in ductile metals: a reconsideration, Eng. Fract. Mech. 74 (2007) 1344–1359, https://doi.org/10.1016/j.engfracmech.2006.06.011.
[48] K. Lu, Making strong nanomaterials ductile with gradients, Science (80-.) 345 (2014) 1455–1456, https://doi.org/10.1126/science.1255940.
[49] S.C. Cao, J. Liu, L. Zhu, L. Li, M. Dao, J. Lu, R.O. Ritchie, Nature-inspired hierarchical steels, Sci. Rep. 8 (2018) 5088, https://doi.org/10.1038/s41598-018-23358-7.
[50] R. Cao, Q. Yu, J. Pan, Y. Lin, A. Sweet, Y. Li, R.O. Ritchie, On the exceptional damage-tolerance of gradient metallic materials, Mater. Today (2019) https://doi.org/10.1016/j.mattod.2019.09.023.
[51] R. Pippan, F. Riemelmoser, C. Bichler, Measurability of crack closure, Adv. Fatigue Crack Clos. Meas. Anal. Second Vol. ASTM International, 100 Barr Harbor Drive, PO Box C700, West Conshohocken, PA 19428-2959, 1999https://doi.org/10.1520/STP15749S , (pp. 41-41–16).
[52] M.W. Kapp, O. Renk, T. Leitner, P. Ghosh, B. Yang, R. Pippan, Cyclically induced grain growth within shear bands investigated in UFG Ni by cyclic high pressure torsion, J. Mater. Res. 32 (2017) 4317–4326, https://doi.org/10.1557/jmr.2017.273.
[53] B. Yang, H. Vehoff, A. Hohenwarter, M. Hafok, R. Pippan, Strain effects on the coarsening and softening of electrodeposited nanocrystalline Ni subjected to high pressure torsion, Scr. Mater. 58 (2008) 790–793, https://doi.org/10.1016/j.scriptamat.2007.12.039.
[54] J. Luo, K. Ying, P. He, J. Bai, Properties of Savitzky–Golay digital differentiators, Digit. Signal Process. 15 (2005) 122–136, https://doi.org/10.1016/j.dsp.2004.09.008.
[55] Jianwen Luo, Jing Bai, Ping He, Kui Ying, Axial strain calculation using a low-pass digital differentiator in ultrasound elastography, IEEE Trans. Ultrason. Ferroelectr. Freq. Control. 51 (2004) 1119–1127, https://doi.org/10.1109/TUFFC.2004.1334844.
[56] B. Pan, A. Asundi, H. Xie, J. Gao, Digital image correlation using iterative least squares and pointwise least squares for displacement field and strain field measurements, Opt. Lasers Eng. 47 (2009) 865–874, https://doi.org/10.1016/j.optlaseng.2008.10.014.